High-speed wide dynamic range linear mode time-of-flight receiver based on zero-crossing timing detection

Aram Baharmast◉* and Juha Kostamovaara
University of Oulu, Faculty of Information Technology and Electrical Engineering,
Circuits and Systems Research Unit, Oulu, Finland

Abstract. We present an accurate laser radar receiver with a wide dynamic range intended for ranging applications based on an event-based approach, in which a receiver-time-to-digital converter is used to extract the timing information from the reflected echo. The receiver is based on LC resonance pulse shaping at the input so that the unipolar pulse detected by the avalanche photodiode is converted to a bipolar signal, and the first zero-crossing of this converted signal is marked as the only timing point. One important aspect of the proposed scheme is that it does not need any postcompensation or gain control for achieving a wide dynamic range. The receiver chip was fabricated in a 0.35-μm standard CMOS technology, and a laser radar platform was developed to verify the functionality of the proposed receiver channel. The measured accuracy of the receiver is ± 3.5 cm within a dynamic range of more than 1:250,000 using 3-ns FWHM pulses when target materials with different reflectivities are used in the measurements. The single-shot precision of the receiver (σ value) is ~5 cm for a minimum SNR of ~10. © *The Authors. Published by SPIE under a Creative Commons Attribution 4.0 Unported License. Distribution or reproduction of this work in whole or in part requires full attribution of the original publication, including its DOI.* [DOI: 10.1117/1.OE.59.10.104102]

1 Introduction

Laser ranging devices have many well-established applications in industry, traffic control, farming, geodesy, and airborne laser scanning.[1–3] Nowadays, these devices are even more attractive due to their important role in self-driving cars, drones, consumer electronics (games), robotics, and gesture control, for example.[4–6]

Optical time-of-flight (TOF) laser ranging devices can be characterized as either direct or indirect (iTOF versus dTOF),[7,8] with both techniques employed in a wide variety of applications. In iTOF method, an amplitude-modulated light carrier is emitted to the target, and the distance is resolved from the phase difference between the transmitted and received signal echoes. This technique can achieve a high level of accuracy in short-range applications,[9] but it suffers from a limited unambiguous measurement range, which is directly dependent on the modulation frequency employed ($R_{\max} = c/2\,f$, where c is the speed of light and f is the modulation frequency), which is typically in the range 10 to 100 MHz.[10,11] To mitigate this, either the carrier frequency should be reduced, which would, in turn, sacrifice the precision, or else several carrier frequencies should be employed, at the cost of greater complexity.[12] This problem does not affect the dTOF technique (also known as pulsed TOF), where the distance is resolved directly from the round-trip time of the laser pulse to the target and back to the receiver, owing to the fact that the pulsing rate is typically in the range of tens to hundreds of kHz. Furthermore, in this method, the optical power of the laser can be concentrated into the moment of timing (contrary to modulated continuous emission) so that cm-level (or even mm level) precision can be achieved even in a single measurement.[11,13,14] Here, dTOF approach is followed.

---

*Address all correspondence to Aram Baharmast, aram.baharmast@oulu.fi

The two detection modes employed in pulsed TOF receivers are single-photon detection and linear detection mode, each dealing with different challenges. In the single-photon detection mode (i.e., Geiger mode), the photodetector, which is a variant of avalanche photodiode (APD) is reverse-biased above its breakdown voltage. Therefore, absorption of a single photon in its depletion region may result in an avalanche breakdown and a digital-like signal.[15] With recent advances in integrated single photon avalanche photodiode (SPAD), this approach has shown great potential in three-dimensional (3D) imaging, especially in near-range applications.[16] However, dark current and background-induced noise, which may completely block the receiver, is a problem in receivers of this type. This issue can be addressed by employing an array of SPADs to detect multiple echoes per laser pulse and/or time gating of SPADs (active quenching) to lower the noise triggering probability in collaboration with a multichannel time-to-digital converter (TDC).[17,18] These techniques may complicate the design of the receiver, however.

In the linear detection mode, the photodetector, which is usually an APD or PIN, is biased below the breakdown voltage and produces current pulses proportional to the received optical power.[15,19] In these receivers, the background illumination does not block signal detection but instead adds extra noise to the input of the receiver. The dominant noise source, especially at low signal levels, is nevertheless the noise due to the receiver electronics itself, which defines the limit of sensitivity in many cases, especially around 900-nm wavelength region where the dark current noise of the APD is lower than 1550-nm wavelength.[20] Therefore, low noise techniques should be employed in the design of the receiver front end. Another challenge associated with such receivers is the considerable variation in the amplitude of the received sub-10-ns pulse, which translates into timing walk error. This is a systematic error that has two main sources.[21] The first one of these, known as geometric walk error, is variation in the pulse rise time at the timing moment with the change in the pulse amplitude. This exists even with an ideal comparator. The other source is the nonlinear propagation delay of the receiver electronics for varying pulse amplitudes.[22] Shown in Fig. 1(a), the total walk error in ranging applications can be as large as several nanoseconds with the typical nanosecond (ns) range pulse width used (66 ps ≡ 1 cm).[17]

One successful way to tackle this issue is to sample the echo signals continuously and convert them to digital data using an analog-to-digital converter (ADC).[23,24] In this way, walk error-free time positions of the reflected echoes can be acquired. However, since short ns-range laser pulses are typically used, this technique needs high sampling rates of several hundred megahertz and a multibit ADC for accurate detection, which in turn entails power consumption problems, especially in multichannel realizations.[25]

In another trending technique, known as the event-based approach, a TDC is employed to measure the time interval between the start pulse of the laser and the echo reflected from the target. The TDC is triggered only when a sufficiently powerful signal is detected that exceeds the noise by a certain margin. This technique allows low power and highly integrated realization of the laser radar, which is especially vital in 2D/3D applications. Interdisciplinary approaches based on both the above-mentioned techniques have also been proposed recently (see Refs. 7 and 26).

In the event-based approach, where continuous sampling of the reflected echoes is not available, a walk error compensation scheme should be conceived for accurate positioning of the
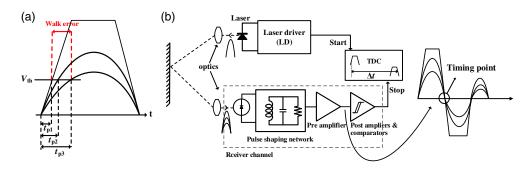

Fig. 1 (a) Conceptual diagram of the walk error. (b) Event-based laser radar using pulse-shaping at the input of the receiver channel.

timing point. This is essential because, in ranging applications, the reflected echo may vary over a wide dynamic range of 1:10,000 or even more, depending on the reflectance properties of the target, the distance range, and weather conditions. One possible way to tackle this issue is to employ optical (mechanically moving) or electrical gain control to ensure that the receiver channel is always in its linear region (see Refs. 14, 27, 28, and references therein). The former is usually slow and bulky, however, and consumes a lot of power, whereas the latter can typically cover a narrow dynamic range. Although recent implementations of this technique have achieved a reported dynamic range of more than 1:2000, the walk error has still been relatively large, e.g., 1 ns,[29,30] due to nonconstant electronic propagation delay in each gain mode. Another method is to employ constant fraction time discrimination in which the timing moment is located at a constant fractional point of the leading edge of the analog pulse. In this technique, the input pulse is usually divided into a delayed and an attenuated pulse. The timing moment is the point in which the delayed pulse crosses the top (or near the top) of the attenuated pulse.[31–33] Although, this works properly only within the linear dynamic range of the receiver channel, which in modern IC technology nodes is inevitably narrow ($<1:100\ldots200$).[14] One successful approach for covering a wide DR (e.g., more than 1:10,000) while keeping the walk error at a low level (e.g., 50 ps) is to use time-domain compensation techniques, in which various input pulse characteristics such as rise time, width and/or slew rate, RMS value, and/or peak amplitude are fetched and applied to compensate for the walk error.[34–36] These techniques, although effective as such, need calibration, however, which increases the complexity of the laser radar and/or compromises its speed.

Another approach for achieving accurate timing is based on unipolar-to-bipolar pulse shaping at the input to the receiver channel, where the unipolar current pulse from the APD is converted to a bipolar signal. The timing information is extracted from the first zero-crossing point of the converted signal.[37] Shown in Fig. 1(b), this ensures that the variation in the zero-crossing time (i.e., walk error) is kept at a low level, provided that the receiver channel is designed to recover fast enough from clipping in the case of high input amplitude levels and considering that the channel is always linear in the vicinity of the zero-crossing point of the signal. Consequently, a wide dynamic range can be achieved.

We have proposed a new implementation of unipolar-to-bipolar pulse shaping, in which an LC resonator is combined with a nonlinear shunt feedback transimpedance amplifier (TIA) at the input to the receiver channel. One important aspect of this scheme is that it does not require postcompensation or gain control. Therefore, it can lead to a highly integrated and compact realization of the laser radar in collaboration with a single-channel TDC. The receiver circuit has been realized as a custom-designed CMOS IC and its circuit level details, related analysis, and measurements are presented elsewhere.[38–41] This paper presents system-level equations and measurements for the proposed receiver channel when used as part of a pulsed laser radar system. In particular, the relation between the laser transmitter (peak power, pulse width, and rise time) and receiver parameters (bandwidth) and system-level performance (walk error, sensitivity, and jitter) is discussed. A LiDAR (light detection and ranging) environment with a 35-m distance range and target materials covering a wide range of reflectivities was developed to evaluate the performance of the proposed receiver techniques. The performance measurements demonstrate a linearity error of ± 3.5 cm within a dynamic range of more than 1:250,000 without using any postcompensations. Furthermore, it is shown that the proposed technique supports high pulsing rates of up to 4 to 5 MHz.

The paper proceeds as follows: general considerations in the design of a linear mode laser radar will be discussed in Sec. 2, the proposed technique will be described in Sec. 3, Sec. 4 will be devoted to the measurement environment and the results achieved, and conclusions will be drawn in Sec. 5.

2 Laser Radar Architecture and Parameters

A block diagram of a pulsed TOF laser radar based on the linear detection mode is shown in Fig. 1(b) (with the emphasis here on the input pulse shaping technique used in the receiver). The laser driver is typically based on avalanche breakdown in bipolar transistors or high voltage

CMOS-based switches.[42,43] The commercial off-the-shelf drivers can deliver current rates in 10 A/ns regime to produce laser pulses of width 3 to 5 ns and peak optical power levels of 20 to 30 W from double heterostructure semiconductor laser diodes working in the near-infrared wavelength range. With a typical receiver aperture of 2 to 3 cm, this level of power and pulse width is needed for an accurate (cm-level) laser radar for use in ranging applications covering tens of meters to noncooperative (Lambertian type) targets. Shorter (e.g., subnanosecond) pulses are attractive for a high precision laser radar and on the grounds of eye safety. But the readily available driver techniques cannot maintain the same power levels while delivering such short pulses. As will be discussed below, it is the pulse shape that determines the required bandwidth in the linear detection mode and directly affects the timing uncertainty (jitter) in the receiver. Here, a commercial MOS-based driver (ON Semiconductor, FDMC86244) and a commercial semiconductor laser (Laser Components, 905D1S2J03Y) were used to produce optical pulses with 3 ns/1.56 ns pulse width/rise time.

The optical power at the receiver aperture when the target is of the Lambertian noncooperative type can be found using the radar equation:

$$P_R(R) = \frac{P_T \tau_T \tau_R \rho r^2}{R^2} T(R) e^{-2\gamma R}, \tag{1}$$

where P_T is the output power of the laser diode, τ_T and τ_R are the transmissions of the transmitter and receiver optics, respectively, ρ is the reflectivity of the target, r is the radius of the effective aperture of the receiver optics, and R is the target distance. $T(R)$, the overlap function represents the effect of fixed paraxial optics on the received signal level. It can be assumed to be 1 for the ranges in which the detector sees the whole laser spot image and less than 1 for any other cases. The exponential term represents the atmospheric effect. γ is the extinction coefficient and is usually considered to be zero for ranges below hundreds of meters except in the case of the severe atmospheric condition caused by smoke, dust, or smog, for example.[44] The resulting current at the input to the receiver can be found as

$$i_R(R) = P_R(R).R_0, \tag{2}$$

where R_0 is the responsivity of the photodetector. Two commonly used off-chip photodetectors in ranging applications are APD and PIN. APD has the advantage of higher responsivity because of the inherent internal gain (multiplication factor), but this comes with a higher reverse bias requirement. With recent advances in IC technology, on-chip APDs can also be used, which results in a substantial decrease in the input node parasitics (series inductance and parallel capacitance).[45] This feature relaxes the design of high speed (bandwidth) and low noise receiver channel, which are typically required in linear detection mode, but such APDs typically suffer from high dark current noise, high excess noise factor, and limited responsivity (e.g., below 2 A/W). Here, an off-chip APD was used with a typical responsivity of ~35 to 40 A/W at 905 nm wavelength.

The current pulse of the APD resulting from the reflected echo should be strong enough relative to the noise level at the input to the receiver channel so that it can be distinguished. This is defined as the sensitivity limit, and it is known that a minimum SNR of 5 to 10 is required in ranging applications to ensure a negligible false triggering rate.[46] Another limitation tied to the noise is random variation in the timing moment, known as timing jitter. Noise has a considerable effect on timing precision, especially when the signal level is low. The main noise sources on the receiver side are background-induced noise, dark current, and signal-induced current noise from the APD, and noise of the receiver channel. When the signal is weak, however, the latter is typically dominant at ~900-nm wavelength region, and low-noise receiver design techniques need to be employed (especially at the front end). It can be challenging when other design parameters (e.g., the required bandwidth and walk error) must be taken into consideration. This will be discussed in more detail in the next sections.
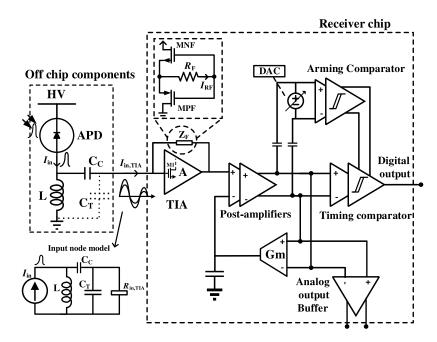
Fig. 2 Block diagram of the proposed receiver channel. TIA, transimpedance amplifier; HV, high voltage; C_T, input node total parasitic capacitance; L, inductance, C_C, coupling capacitor, I_{in}, APD input current; $I_{in,TIA}$, current flowing into the TIA; Z_F, impedance of the TIA feedback path; DAC, digital-to-analog converter; G_m, transconductance amplifier.

3 Receiver Architecture

A block diagram of the proposed receiver channel is shown in Fig. 2. In this scheme, the input circuitry does not include a bias resistor for the APD. Instead, an inductor (L) constructs a resonance network with the parasitic capacitors at the input node (C_T). The current pulse from the APD produces a bipolar voltage signal by passing through the LC resonator and the feedback path of the TIA. A set of postamplifiers are employed to further amplify the output voltage of the TIA to provide enough swing at the input of the timing comparator for the minimum input pulse. The timing comparator converts the amplified signal to full-scale CMOS logic (3.3 V) and sends it outside the receiver chip to trigger the stop channel of the TDC. An arming comparator evaluates the level of the signal and enables the timing comparator only for those signal levels that exceed the noise level by a certain margin. The threshold level of the arming comparator is programmable through a DAC from outside the chip. Apart from the main output, an analog buffer is also placed inside the receiver chip to measure the analog properties of the channel (signal amplitude, BW, gain, and noise). More details on the circuit level implementation of the receiver chip can be found in Refs. 39 and 41.

3.1 Design Parameters of the Front End

The aim is to convert the input unipolar pulse into a bipolar signal at the output of the TIA so that its zero-crossing point does not diverge substantially, even when the large input signal drives the channel into clipping. The fast-transient current pulse of the APD excites the input LC network and an oscillating signal current ($I_{in,TIA}$) is generated. The resulting current flows through the feedback path of the TIA and produces a bipolar voltage signal at the TIA output. Since the only timing information is to be found at the first zero-crossing point of the oscillating signal, a damping oscillation that decays in one or two cycles is needed. The input node consists of a parallel RLC network, the resistance of which (small signal) is equal to

$$R_{in,TI} = \frac{R_F}{A_0 + 1},$$

(3)

where A_0 is the open-loop gain of the core amplifier (A). We assume that the gain-bandwidth product of the core amplifier (GBW) is large enough compared to the frequencies in which the pulse shaping occurs. It is known that in the parallel RLC networks the quality factor (Q) of the circuit roughly indicates the number of cycles of ringing[47] so that the front end RLC circuit can be set to have $Q \approx 1$, which means we should have

$$\sqrt{\frac{L}{C_T}} \approx R_{\text{in,TIA,}} \tag{4}$$

where $Z_{\text{RLC}} \approx \sqrt{L/C_T}$ is the characteristic impedance of the RLC circuit. In this case, the peak-to-peak amplitude of the resulting oscillation at the output of the TIA is equal to

$$V_{\text{out,TIA}} \approx A_0 \sqrt{\frac{L}{C_T}} I_{\text{in}} \approx R_F I_{\text{in}}. \tag{5}$$

Another design guide is the required bandwidth. In general, the rise time of the arriving pulse directly determines the required signal bandwidth[48]

$$\text{BW} \approx \frac{0.35}{t_r}. \tag{6}$$

This is a kind of optimum receiver bandwidth needed to preserve the fast edge of the detected pulse. Therefore, higher bandwidth is required to be able to process shorter pulses. As mentioned earlier, subnanosecond pulses pose practical limits on the LD as well. APDs used in LiDAR typically have a relatively large active area, which in turn results in a high parasitic capacitance at the input node. This is not the only stray element at the input node. Besides, the bonding wire, input PAD, and input transistor of the core amplifier add extra capacitance, so that the pole frequency associated with the input node is the dominant pole of the receiver channel. The -3 dB frequency resulted from this pole is equal to[38]

$$\omega_{-3 \text{ dB}} \cong \frac{A_0 + 1}{2R_F C_T} + \sqrt{\frac{1}{LC_T} + \left(\frac{A_0 + 1}{2R_F C_T}\right)^2}, \tag{7}$$

which is the upper cut-off frequency of the input RLC network. The detailed discussion around stability condition and frequency response of the front end can be found in Ref. 38. According to Eq. (5), a lower input capacitance (C_T) and a larger inductance (L) are to be preferred. For a given C_T however, the value chosen for L cannot be boundlessly high, because it not only limits the bandwidth, as shown in Eq. (7), but also slows down the slew rate of the signal at the timing point, which has a destructive effect on the timing jitter. Therefore $R_{\text{in,TIA}}$ (which sets the damping) should be chosen to be low enough, at which point Z_{RLC} should be matched to it [Eq. (4)]. The value of R_F and A_0 (and therefore the value of $R_{\text{in,TIA}}$) are chosen based on optimized noise and walk error performance. This will be discussed in the next section.

The feedback path consists of two auxiliary transistors (M_{NF} and M_{PF}) and a resistor (R_F). For small input currents, the whole TIA input current ($I_{\text{in,TIA}}$) flows through R_F and the two transistors are switched off. This corresponds to the linear region of the core amplifier. In this case, the input RLC network can be treated as a linear circuit, and the deviation in the zero-crossing for different amplitude levels is negligible. On the other hand, the linear input range is too narrow (e.g., <200 μA) for the typical system-level parameters, due to the limited available voltage headroom in modern IC technology nodes. As the input current exceeds a certain level and drives the core amplifier into the nonlinear region (i.e., A_0 is compressed), the voltage drop across R_F increases, and the two transistors gradually turn on. These transistors modify the impedance of the feedback path (Z_F in Fig. 2) so that it changes as a function of the input current amplitude in the same fashion as A_0. In this way, the effect of nonlinear variation of A_0 on $R_{\text{in,TIA}}$ is canceled out and $R_{\text{in,TIA}}$ remains relatively constant within a wide range of input currents [see Eq. (3)]. This technique can prove useful for increasing the dynamic range of the proposed front

end beyond the linear region of the core amplifier while keeping the walk error at a low level. Further details regarding the function of these transistors can be found in Ref. 41.

3.2 Noise and Timing Jitter

The main contributor to electrical noise in the receiver channel is the feedback resistor (R_F) and the core amplifier of the TIA (especially its input transistor). The thermal noise of the feedback resistor is filtered out by the bandpass LC network, and its total contribution to the RMS noise at the output of the TIA is independent of the value of the feedback resistor itself and depends only on the total input node capacitance (C_T) and the DC gain of the core amplifier (A_0). The noise contribution of the core amplifier is scarcely affected by the input resonance network, however, and should be restricted by limiting its bandwidth. This also applies to the bandwidth of the postamplifiers. This restriction, nevertheless, entails a tradeoff with the walk error, which requires a fast receiver channel that can recover from clipping in the case of high input amplitude levels.[39,40] Consequently, the optimum bandwidth of the amplifiers is set by reference to the desired maximum walk error and noise characteristics.

In the light of the above discussions, a larger R_F is preferred because it results in a greater signal amplitude level [Eq. (5)] while not affecting the total RMS noise. The required damping is then set by A_0 [Eq. (4)]. The final value of A_0 and R_F is nevertheless set based on the optimum bandwidth, walk error, core amplifier noise considerations, and maximum voltage gain that can be achieved using a simple gain stage in the target IC technology node.

The timing uncertainty, i.e., the random variation in the timing moment due to noise, can be approximated by

$$\sigma_t = \frac{\sigma_v}{\left.\frac{\partial V(t)}{\partial t}\right|_{t_p}} \approx \frac{\Delta t_s}{\text{SNR}} \quad \text{and} \quad \sigma_R = \frac{c\Delta t_s}{2\text{SNR}}, \tag{8}$$

where σ_t is the timing uncertainty (jitter), σ_v is the standard deviation of the noise, c is the velocity of light, Δt_s is the slew time of the bipolar signal (approximately from the positive to the negative peak), and $\frac{\partial V(t)}{\partial t}$ is the slope of the signal at the moment of timing, which here is the zero-crossing point. Here, the SNR is defined as the peak-to-peak amplitude of the signal relative to the RMS noise. As can be seen in Eq. (8), the timing uncertainty translates directly into uncertainty in the measured distance. The slew time of the signal can be estimated from the natural frequency of the input RLC network [$\omega_d = \sqrt{\frac{1}{LC_T} - \left(\frac{A_0+1}{2R_F C_T}\right)^2} \approx \frac{0.87}{\sqrt{LC_T}}$]:

$$\Delta t_s \approx \frac{\pi}{2\omega_d} \approx 1.8\sqrt{LC_T}. \tag{9}$$

The approximation given here is based on Eq. (4), whereas the jitter can be roughly estimated based on Eqs. (8) and (9) as

$$\sigma_R = 0.9\frac{c\sqrt{LC_T}}{\text{SNR}}. \tag{10}$$

To improve the jitter, a very large inductance should be avoided, and the parasitic capacitance should be minimized (minimization of C_T relaxes reaching the target bandwidth, for instance, and improves the noise performance of the receiver by minimizing the contribution of high-frequency noise of the core amplifier). The value of C_T is not directly controllable, however, and as mentioned above, a very small inductance also results in a loss in the signal amplitude at the output of the TIA. For the design parameters of 250 nH, 5 kΩ, and 20 for L, R_F, and A_0, respectively, and 4 pF for the total input capacitance C_T, the total input-referred RMS noise was measured to be ~70 nA. In this case, the resonance frequency of the input LC network is equal to ~160 MHz (1 Grad/s) and a rough estimate of the jitter for the minimum SNR of 5, for example, would be ~360 ps, or 5.4 cm in distance.

3.3 *Maximum Pulsing Rate and Measurement Speed*

The pulsing rate of the laser radars in ranging applications is usually restricted by the maximum pulsing rate of the laser driver, which is limited by thermal issues. Also, the receiver may limit the maximum pulsing rate.

One factor restricting the pulsing rate in the receiver is the APD biasing network when accoupled. In some cases, the bias configuration employed at the input to the receiver includes a resistor network (R_{BIAS}) to bias the APD and relatively large capacitors (C_C) to couple the APD to the input node of the receiver channel. The bias resistances are typically chosen to be large enough to ensure that their noise contribution to the input node is lower than that of the receiver channel. In high-sensitivity receivers, where a very low noise level is necessary, the noise component of these resistors cannot be neglected. This configuration imposes a maximum pulsing rate limit on the receiver because, after the arrival of each pulse, the capacitor should return to its initial condition. Otherwise, the detection of the next pulse will be corrupted. This limit can be evaluated by measuring the time constant of the RC network described ($\tau_{\mathrm{input}} = R_{\mathrm{BIAS}}C_C$), where a period of $5\tau_{\mathrm{input}}$ is needed for the settling of more than 99%. It should be noted that the total recovery time also depends on the maximum input current amplitude.

In our case, after the pulse detection/conversion (one or two cycles of ringing), the inductor can be regarded approximately as a short circuit in the recovery time, whereupon the input time constant is $\tau_{\mathrm{input}} \approx R_{\mathrm{in,TIA}}C_C$, where $R_{\mathrm{in,TIA}} \ll R_{\mathrm{BIAS}}$, which means that the speed limit that arose from the input time constant is transformed to a much higher level. Here a coupling capacitor of 70 pF is used, and according to the design parameters, the input resistance of the TIA is always <300 Ω. Therefore, the input time constant is ~21 ns. Our simulations and measurements show that the total maximum recovery time needed in the case of a strongly saturated channel ($I_{\mathrm{in}} > 100$ mA) is about 200 to 250 ns. Consequently, a pulsing rate up to 4 to 5 MHz can be achieved. Figure 3 shows the receiver channel response to three different input current levels (25, 100, and 200 mA), in which the channel is heavily in clipping mode. As can be seen, the channel returns to its initial state within <250 ns in all the cases.

Another source for the speed limit in the linear mode receivers is the need for postprocessing to achieve a certain level of accuracy. The only timing information to be discriminated in the proposed scheme, however, is the first zero-crossing point so that the need for postprocessing to compensate for the timing walk error is eliminated and the complexity of the receiver is reduced.
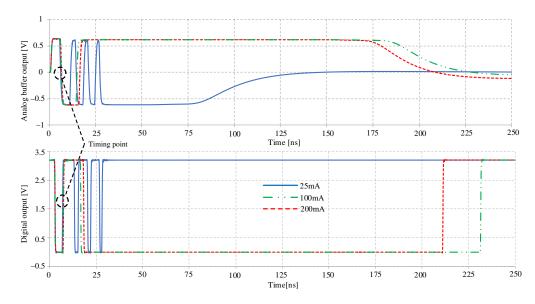

Fig. 3 Simulated transient response of the receiver channel when the input current levels are 25, 100, or 200 mA.

4 Measurement Setup and Results

4.1 *Measurement Platform*

The receiver channel described here was designed and fabricated in a 0.35-μm standard CMOS technology, and a LiDAR environment was developed to evaluate its system-level performance, as shown in Fig. 4.

The semiconductor laser used in the measurements conforms to the following specifications: its emitting stripe width is 75 μm, and it delivers pulses of ~3 ns FWHM in 905 nm wavelength with a peak optical power of ~10 W (measured after the optics). The optical output pulse of the laser, as measured with a broadband optical probe, is shown in Fig. 5(a). The rise time of the pulse when the bandwidth of the measurement oscilloscope is set to 250 MHz (close to the bandwidth of the receiver channel) is about 1.56 ns. The chosen pulse shape matches the bandwidth of the receiver channel (230 MHz), according to Eq. (6).[41] A sample of laser diode current pulses was used to trigger the start channel of the TDC, as shown in Fig. 4.

The focal lengths of the paraxial optics used for the transmitter and receiver sides are 30 and 20 mm, respectively. Therefore, the corresponding divergence of the laser beam is ~2.5 mrad, which gives a spot size of ~7.5 cm at a distance of 30 m. The APD is AD230-8 TO52S1 (First Sensor), with an active area diameter of 230 μm. Its typical responsivity at a wavelength of
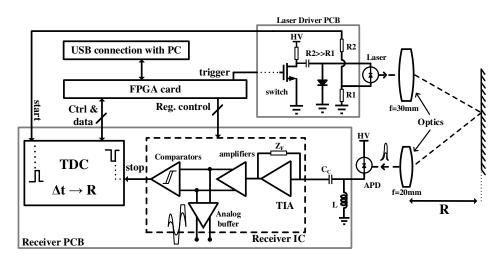

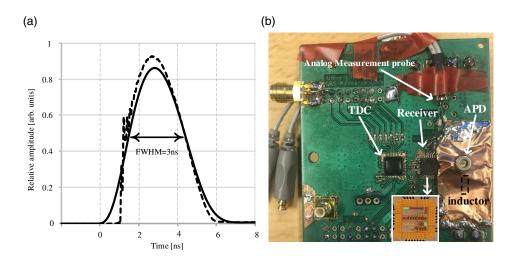**Fig. 4** Block diagram of the developed laser radar.

Fig. 5 (a) Optical pulse of the laser measured using a high bandwidth optical probe (solid line) and the same pulse when the bandwidth of the measurement oscilloscope was set to 250 MHz (dashed line). (b) The receiver PCB.

905 nm is about 35 to 40 A/W when biased close to its breakdown voltage, and its internal gain is ~100. The reverse bias voltage of the APD was set to 138 V in these measurements, which yields enough internal gain for the intended measurement range (35 m), although the reverse bias can be increased to higher voltages (e.g., 150 V).

The receiver channel and the TDC were installed on a single PCB, as shown in Fig. 5(b). The inductor (L) is an off-chip high frequency 250-nH inductor (0603HP25). A two-channel TDC with the ability to measure several pulse characteristics with ~10-ps resolution was employed in the measurements.[49] Only one stop channel in a simple edge measurement mode was used here, however. The whole transmitter PCB and the input node of the receiver were shielded using a thin copper sheet in order to minimize disturbances in the receiver channel resulting from the high-speed driving current of the laser and other switching activities of the digital parts (e.g., the TDC and the digital output of the receiver). An analog probe was attached to the receiver PCB to measure the amplitude of the signal in the channel, as shown in Fig. 5(b). A Verilog-based program was developed to control the measurement process and communicate with the PC using an XEM6001 Xilinx FPGA. All the measurements were performed at room temperature under indoor light conditions (background radiation <50 lx).

The measured total transimpedance gain (peak-to-peak output voltage amplitude per input current pulse amplitude), channel bandwidth, and input-referred current (floor) noise are ~1.2 MΩ, ~230 MHz, and ~70 nA RMS, respectively. More details on these measurements are provided in Ref. 41. The dark current of the APD is specified to be 0.2 to 0.5 nA (at its anode). Thus, its corresponding noise current at the input of the receiver is ~2 to 3 nA RMS [internal gain $M = 100$, excess noise factor $F(M) = 2.2$, bandwidth BW = 230 MHz], which is negligible when compared to the total current noise of the receiver.

The laser radar described here was installed on an automated measurement track to characterize the performance of the proposed receiver channel. The track sweep range was 35 m, and its target locating accuracy was better than ±0.5 mm. The laser radar was focused on 35 m to maximize the overlap function within the distance range. As can be seen next, however, due to biaxial optics, this condition was met for distance ranges above 5 m. Two sets of measurements were performed: intensity and linearity measurements, as detailed below, employing three targets representing different levels of reflectivity: black cardboard ($\rho = 12\%$), white paper ($\rho = 100\%$), and reflective diamond grade sheet, whose angular reflectivity along the optical axis of the radar is ≫100% (greater than that of the white paper) due to specular reflection. The first two are considered diffuse reflecting (Lambertian type) targets, and the latter is a retro-reflector. The given reflectivity values are based on the reflectivity of the white (copy) paper as provided in Ref. 50 for ~900-nm wavelength.

Typical analog output signals as measured from the analog buffer and their corresponding digital output (from the comparator) are shown in Fig. 6. In these measurements, the target was located at ~21 m from the laser radar. The corresponding input current amplitudes for the black cardboard, white paper, and diamond grade sheet (with a 42% transmittance filter) were about 2.25 μA, 17 μA, and 26 mA, respectively. Even though they corresponded to quite different ranges of currents, the pulse shaping was carried out for all the targets, as can be seen, and their timing moments (trailing edge) lay within a close time interval. In the case of the 26 mA input current, in which the receiver channel was intensively in the clipping mode (comparable to the simulation case shown in Fig. 3 for 25-mA input current), the channel returned to its initial condition in ~160 ns (from 130 to ~290 ns). The fast decaying ringing seen around 280 ns may have occurred because of some other disturbances in the circuit, but it did not interfere with the timing moment, which had happened earlier. As can be seen, the weaker signal resulted in a narrower output pulse, which is because of the structure of the arming comparator (for more details, see Ref. 41). It should be taken into consideration since the TDC used here can only measure timing pulses with a width greater than ~1 ns.

4.2 Intensity Measurements

The purpose of the intensity measurements is to identify the equivalent input optical pulse variations (dynamic range) for each target type when the target was swept on the track in 0.5 to 1 m steps. The reason to use target materials with different reflectivity, as will be evident next, was
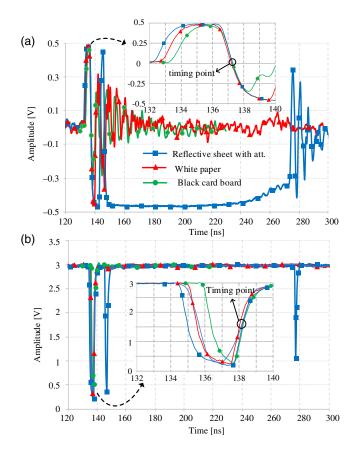
Fig. 6 Sample outputs measured from (a) the analog output buffer and (b) digital output from the comparator.
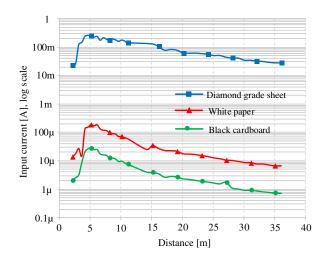

Fig. 7 Measured input currents for different target types when the target was swept along the track.

to supply a wide dynamic range of the input optical pulses, considering that the sweep range of the track was limited to 35 m.

In these measurements for each target material, the peak-to-peak amplitude of the analog buffer output was recorded for each distance point. Simultaneously, the receiver channel was kept in its linear region employing neutral density filters (which their transmittance at 905 nm wavelength was known). Since the transimpedance gain of the channel was also known (1.2 MΩ), the equivalent input current could be calculated. The results are shown in Fig. 7.

As can be seen, by sweeping the targets with different reflectivities in the 35-m distance range, a dynamic range of at least 1∶300,000 is explored. In other words, from ∼0.8 μA for the black cardboard at 35 m to ∼260 mA for the diamond grade sheet at ∼5 m. The linearity of the receiver channel was examined in this dynamic range, as detailed below. The sudden decrease in the input current when the target was too close to the laser radar (<3 m) was because of the biaxial (fixed) optics used the field of view of the receiver optics covers only a small portion of the laser image spot. As mentioned in Sec. 2, in this region, the overlap function decreases substantially, and the received optical power shrinks.

4.3 Linearity Measurements

Once that the intensity of the arrived optical pulse for each target, hence their relative position in the dynamic range was known, the linearity of the receiver could be studied by sweeping the target and recording the travel time of the optical pulse using the TDC. The purpose of this measurement is to identify the accuracy of the receiver channel when the intensity of the input optical pulse varies in a wide dynamic range. For each point, 6000 measurements were performed to reach a reliable statistical accuracy. The recorded time intervals were then translated into the distance, by reference to the speed of light. The linearity error was defined as the difference between the real distance (recorded from the calibrated track) and the measured distance for each measurement point. The results are shown in Fig. 8. The curves were fitted according to the average linearity error for the white paper (i.e., the average linearity error for the white paper in the 2- to 35-m measurement range was set to zero). For the diamond grade sheet, two sets of tests were performed, one without any attenuation filter (continuous blue curve) and the other with a 75% transmittance filter in front of the receiver lens (dashed blue curve). According to Fig. 7 in the former case, the input current varies in a range of 260 mA∶28 mA and therefore ∼195 mA∶21 mA in the latter case.

As shown in Fig. 8, in the case of the diamond grade sheet without attenuation, the linearity error is maximum and peaks at ∼5 m distance with a 3.5-cm error. In all the other cases that correspond to ∼0.8 μA∶195 mA input current range (dynamic range more than 1∶200,000), the linearity error is less than ±1.5 cm. This error is not only due to the walk error resulting from the nonlinearity of the receiver electronics. The quality of the optics and possibly small variation in the overlap function when the distance varies from 3 to 35 m also affects the total error seen in the receiver.

4.4 Single-Shot Precision and Jitter

The single-shot precision of a laser radar device can be evaluated by measuring the distribution of single-shot measurements obtained at different input power levels. The distribution of single-
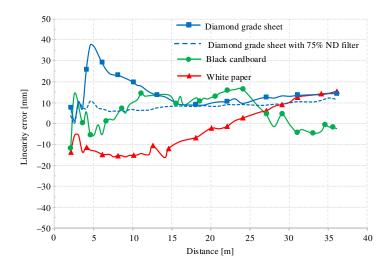

Fig. 8 Nonlinearity of the receiver channel for different target materials.
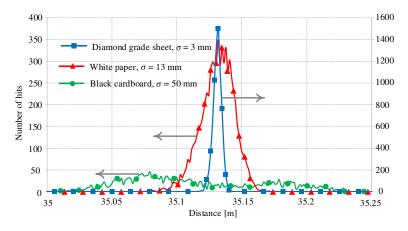
Fig. 9 Distribution of measured time interval hits (translated to distance) at ~35.12 m distance. The corresponding SNRs for the black cardboard, white paper, and diamond grade sheet were ~10, 93, and >10,000, respectively.

shot time intervals when the target was at 35 m (maximum track distance) is shown in Fig. 9. In the case of the black cardboard, the reflected echo is almost at its minimum level ($I_{in} \approx 0.8$ μA, equivalent to SNR ≈ 10, according to Fig. 7). As can be seen, the detected stop hits do not follow a normal distribution in this case, which is probably due to an electric disturbance that modulates the timing point. This disturbance is dominant only when the signal level and, therefore, the slew rate of the signal is low. In the case of the white paper ($I_{in} \approx 6.5$ μA, equivalent to SNR $= 93$), the hits follow a normal distribution, and the jitter is 13 mm (σ value), whereas the measured jitter in the case of the diamond grade sheet was at its minimum level of ~3 mm not only at 3 5 m distance but also over the whole track range. This was because, in this case, the channel was always intensely saturated by the very large input current. Consequently, the jitter reaches its minimum level, which is defined by the maximum slew rate of the signal, the signal-induced current noise of the APD, and the limited precision of the TDC (10 ps equals to 1.5 mm in distance) and the measurement setup.

5 Conclusion

This paper presents the development and testing of a receiver chip intended for pulsed TOF laser radars operating based on the linear detection mode. The receiver employs a unipolar-to-bipolar pulse shaping technique at the input to the receiver, where the timing position of the arriving echo is found from the first zero-crossing point of the converted bipolar signal. A LiDAR environment was developed to test various characteristics of the receiver channel using a laser that delivers a peak power of 10 W and pulse width of 3-ns FWHM. The measurements, obtained by sweeping target materials with different reflectivities from 3 to 35 m, show that the nonlinearity error of the receiver is less than ± 3.5 cm for a dynamic range of more than 1:250,000 (± 1.5 cm for the dynamic range of 1:200,000 starting from the minimum signal). The measured single-shot precision for the worst-case scenario (black cardboard located at a maximum distance of 35 m) was ~50 mm at an SNR of 10. In this case, a crosstalk between the high-speed digital output side of the receiver and the sensitive analog input side modulates the timing point when the signal amplitude approaches its minimum levels. This issue can be mitigated by further minimizing the noise at the input to the arming comparator and using isolation techniques in the layout phase of the receiver design. The single-shot precision was 13 mm for the white paper (SNR $= 90$) and 3 mm for the diamond grade sheet (SNR $> 10,000$) both at 35 m distance.

Our measurements have demonstrated the capability of the proposed receiver technique to cover a wide dynamic range of optical pulse amplitudes without using a complicated receiver topology. The measurement range of the laser radar can be increased simply by increasing the peak power of the laser or, as mentioned, by increasing the internal gain of the APD. The proposed receiver does not need any walk compensation or gain control (to keep the receiver

channel in the linear region) to achieve such an extensive dynamic range. Furthermore, due to its simple structure, the receiver supports high pulsing rates of up to 4 to 5 MHz. These features enable the use of the receiver in high speed/precision applications, where several rounds of measurement may be needed to reach a certain precision level. Thus, the proposed receiver can pave the way to be used in 2D (line profilers) or 3D range imager devices, for example.

Acknowledgments

References

1. C. Mallet and F. Bretar, "Full-waveform topographic lidar: state-of-the-art," *ISPRS J. Photogramm. Remote Sens.* **64**(1), 1–16 (2009).
2. M. Amann et al., "Laser ranging: a critical review of unusual techniques for distance measurement," *Opt. Eng.* **40**(1), 10–19 (2001).
3. S. Donati, *Electro-Optical Instrumentation: Sensing and Measuring with Lasers*, Pearson Education, London (2004).
4. V. C. Coffey, "Imaging in 3-D: killer apps coming soon to a device near you!" *Opt. Photonics News* **25**(6), 36–43 (2014).
5. B. Behroozpour et al., "Lidar system architectures and circuits," *IEEE Commun. Mag.* **55**(10), 135–142 (2017).
6. X. Mao et al., "Amplitude-modulated laser radar for range and speed measurement in car applications," *IEEE Trans. Intell. Transp. Syst.* **13**(1), 408–413 (2012).
7. M. Liu et al., "A 60-m range 6.16-mW laser-power linear-mode LiDAR system with multiplex ADC/TDC in 65-nm CMOS," *IEEE Trans. Circuits Syst. I Regul. Pap.* **67**(3), 753–764 (2020).
8. R. Horaud et al., "An overview of depth cameras and range scanners based on time-of-flight technologies," *Mach. Vision Appl.* **27**(7), 1005–1020 (2016).
9. L. Gatet et al., "Surface detection using a phase-shift laser range finder and neural network," *Opt. Eng.* **46**(7), 073002 (2007).
10. J. F. Munro, "Low-cost laser rangefinder with crystal-controlled accuracy," *Opt. Eng.* **44**(2), 023605 (2005).
11. M. Koskinen, J. T. Kostamovaara, and R. A. Myllylae, "Comparison of continuous-wave and pulsed time-of-flight laser range-finding techniques," *Proc. SPIE* **1614**(1), 296–305 (1992).
12. S. Poujouly and B. Journet, "A twofold modulation frequency laser range finder," *J. Opt. A* **4**(6), S356 (2002).
13. J. M. Rüeger, *Electronic Distance Measurement: An Introduction*, Springer Science & Business Media, Berlin, Germany (1996).
14. T. Ruotsalainen, P. Palojarvi, and J. Kostamovaara, "A wide dynamic range receiver channel for a pulsed time-of-flight laser radar," *IEEE J. Solid-State Circuits* **36**(8), 1228–1238 (2001).
15. P. F. McManamon et al., "Comparison of flash lidar detector options," *Opt. Eng.* **56**(3), 031223 (2017).
16. S. Jahromi et al., "A 32 × 128 SPAD-257 TDC receiver IC for pulsed TOF solid-state 3-D imaging," *IEEE J. Solid-State Circuits* **55**, 1960–1970 (2020).
17. J. Kostamovaara et al., "On laser ranging based on high-speed/energy laser diode pulses and single-photon detection techniques," *IEEE Photonics J.* **7**(2), 1–15 (2015).
18. J. Huikari et al., "Compact laser radar based on a subnanosecond laser diode transmitter and a two-dimensional CMOS single-photon receiver," *Opt. Eng.* **57**(2), 024104 (2018).
19. A. Ullrich and M. Pfennigbauer, "Linear LIDAR versus Geiger-mode LIDAR: impact on data properties and data quality," *Proc. SPIE* **9832**, 983204 (2016).
20. G. M. Williams, Jr., "Optimization of eyesafe avalanche photodiode lidar for automobile safety and autonomous navigation systems," *Opt. Eng.* **56**(3), 031224 (2017).

21. J. Kostamovaara et al., "On the minimization of timing walk in industrial pulsed time-of-flight laser radars," *Proc. SPIE* **7356**(1), 73560N (2009).

22. R. J. van de Plassche and P. Baltus, "An 8-bit 100-MHz full-Nyquist analog-to-digital converter," *IEEE J. Solid-State Circuits* **23**(6), 1334–1344 (1988).

23. T.-H. Ngo et al., "Wideband receiver for a three-dimensional ranging LADAR system," *IEEE Trans. Circuits Syst. I Regul. Pap.* **60**(2), 448–456 (2013).

24. C. Li et al., "Laser time-of-flight measurement based on time-delay estimation and fitting correction," *Opt. Eng.* **52**(7), 076105 (2013).

25. "LIDAR-pulsed time-of-flight reference design using high-speed data converters," TI Designs: TIDA-01187, Texas Instruments (2016).

26. K. Yoshioka et al., "A 20-ch TDC/ADC hybrid architecture LiDAR SoC for 240 × 96 pixel 200-m range imaging with smart accumulation technique and residue quantizing SAR ADC," *IEEE J. Solid-State Circuits* **53**(11), 3026–3038 (2018).

27. R. Ma et al., "A 77-dB dynamic range low-power variable-gain transimpedance amplifier for linear LADAR," *IEEE Trans. Circuits Syst. II* **65**(2), 171–175 (2018).

28. R. Ma et al., "A 66-dB linear dynamic range, 100-dB Ω transimpedance gain TIA with high-speed PDSH for LiDAR," *IEEE Trans. Instrum. Meas.* **69**(4), 1020–1028 (2020).

29. H. Zheng et al., "A linear dynamic range receiver with timing discrimination for pulsed TOF imaging LADAR application," *IEEE Trans. Instrum. Meas.* **67**(11), 2684–2691 (2018).

30. H. Zheng et al., "High sensitivity and wide dynamic range analog front-end circuits for pulsed TOF 4-D imaging LADAR receiver," *IEEE Sens. J.* **18**(8), 3114–3124 (2018).

31. A. Kilpelä et al., "Timing discriminator for pulsed time-of-flight laser range finding measurements," *Rev. Sci. Instrum.* **69**(5), 1978–1984 (1998).

32. D. A. Gedcke and W. J. McDonald, "Design of the constant fraction of pulse height trigger for optimum time resolution," *Nucl. Instrum. Methods* **58**(2), 253–260 (1968).

33. M. L. Simpson et al., "An integrated, CMOS, constant-fraction timing discriminator for multichannel detector systems," *IEEE Trans. Nucl. Sci.* **42**(4), 762–766 (1995).

34. S. Kurtti, J. Jansson, and J. Kostamovaara, "A CMOS receiver-TDC chip set for accurate pulsed TOF laser ranging," *IEEE Trans. Instrum. Meas.* **69**(5), 2208–2217 (2020).

35. J. Nissinen, I. Nissinen, and J. Kostamovaara, "Integrated receiver including both receiver channel and TDC for a pulsed time-of-flight laser rangefinder with cm-level accuracy," *IEEE J. Solid-State Circuits* **44**(5), 1486–1497 (2009).

36. P. Palojarvi, T. Ruotsalainen, and J. Kostamovaara, "A 250-MHz BiCMOS receiver channel with leading edge timing discriminator for a pulsed time-of-flight laser rangefinder," *IEEE J. Solid-State Circuits* **40**(6), 1341–1349 (2005).

37. J. Pehkonen, P. Palojarvi, and J. Kostamovaara, "Receiver channel with resonance-based timing detection for a laser range finder," *IEEE Trans. Circuits Syst. I Regul. Pap.* **53**(3), 569–577 (2006).

38. A. Baharmast and J. Kostamovaara, "A low noise front end trans-impedance amplifier channel for a pulsed time-of-flight laser radar," in *13th Conf. PhD Res. Microelectron. and Electron.*, pp. 285–288 (2017).

39. A. Baharmast, T. Ruotsalainen, and J. Kostamovaara, "A low noise, wide dynamic range TOF laser radar receiver based on pulse shaping techniques," in *IEEE Int. Symp. Circuits and Syst.*, pp. 1–5 (2018).

40. A. Baharmast and J. Kostamovaara, "Noise considerations in pulse-shaping based TIA channel designed for a pulsed TOF laser radar receiver," in *IEEE Nordic Circuits and Syst. Conf.: NORCHIP and Int. Symp. Syst.-on-Chip*, pp. 1–6 (2018).

41. A. Baharmast, S. Kurtti, and J. Kostamovaara, "A wide dynamic range laser radar receiver based on input pulse-shaping techniques," *IEEE Trans. Circuits Syst. I* **67**(8), 2566–2577 (2020).

42. L. Hallman, J. Huikari, and J. Kostamovaara, "A high-speed/power laser transmitter for single photon imaging applications," in *IEEE Sensors*, pp. 1157–1160 (2014).

43. A. Kilpelä and J. Kostamovaara, "Laser pulser for a time-of-flight laser radar," *Rev. Sci. Instrum.* **68**(6), 2253–2258 (1997).

44. K. Määtta, J. Kostamovaara, and R. Myllylä, "Profiling of hot surfaces by pulsed time-of-flight laser range finder techniques," *Appl. Opt.* **32**(27), 5334–5347 (1993).

45. A. Chowdhury, R. F. Karlicek, and M. M. Hella, "A monolithically integrated time-of-flight sensor with large area silicon avalanche photodiode," in *IEEE 62nd Int. Midwest Symp. Circuits and Syst.*, pp. 1203–1206 (2019).
46. H. N. Burns, C. G. Christodoulou, and G. D. Boreman, "System design of a pulsed laser rangefinder," *Opt. Eng.* **30**(3), 323–329 (1991).
47. T. H. Lee, *The Design of CMOS Radio-Frequency Integrated Circuits*, Cambridge University Press, Cambridge (2003).
48. R. E. Ziemer and W. H. Tranter, *Principles of Communications: System Modulation and Noise*, John Wiley & Sons, Hoboken, New Jersey (2014).
49. J.-P. Jansson, A. Mantyniemi, and J. Kostamovaara, "A CMOS time-to-digital converter with better than 10 ps single-shot precision," *IEEE J. Solid-State Circuits* **41**(6), 1286–1296 (2006).
50. RIEGL, "Reflectivity of various surfaces/materials," Laser measurement systems, Application Note AN-GI004, RIEGL (2009).

Aram Baharmast received his MSc degree in electronics from Iran University of Science and Technology, Tehran, Iran, in 2013. He joined the Circuits and Systems research unit (CAS) of the University of Oulu in 2016 where he has been pursuing his Dr. Tech. in electronics. His main research interests include mixed signal integrated circuits and systems for the development of pulsed time-of-flight (TOF) laser rangefinders.

Juha Kostamovaara received his Dr Eng (electrical engineering) degree from the University of Oulu, Oulu, Finland, in 1987. He held the Academy professorship position nominated by the Academy of Finland from 2006 to 2011 and then for a second time from 2012 to 2017. Currently, he holds a professorship in electronics at the University of Oulu (CAS). His main research interests are the development of pulsed TOF devices, circuits, and systems for electronic and optoelectronic measurements.